This is the accepted manuscript made available via CHORUS. The article has been published as:

Anisotropy of antiferromagnetic domains in a spin-orbit Mott insulator

Longlong Wu, Wei Wang, Tadesse A. Assefa, Ana F. Suzana, Jiecheng Diao, Hengdi Zhao, Gang Cao, Ross J. Harder, Wonsuk Cha, Kim Kisslinger, Mark P. M. Dean, and Ian K. Robinson

Phys. Rev. B **108**, L020403 — Published 20 July 2023

DOI: 10.1103/PhysRevB.108.L020403

Anisotropy of Antiferromagnetic Domains in a Spin-orbit Mott Insulator

Longlong Wu[1*], Wei Wang[1], Tadesse A. Assefa[1,2], Ana F. Suzana[1], Jiecheng Diao[3], Hengdi Zhao[4], Gang Cao[4], Ross J. Harder[5], Wonsuk Cha[5], Kim Kisslinger[6], Mark P. M. Dean[1] and Ian K. Robinson[1,3†]

[1]*Condensed Matter Physics and Materials Science Department, Brookhaven National Laboratory, Upton, NY 11973, USA*

[2]*Stanford Institute for Materials and Energy Sciences, SLAC National Accelerator Laboratory, Menlo Park, California 94025, USA*

[3]*London Centre for Nanotechnology, University College London, London, WC1E 6BT, United Kingdom.*

[4]*Department of Physics, University of Colorado at Boulder, Boulder, Colorado 80309, USA*

[5]*Advanced Photon Source, Argonne National Laboratory, Illinois 60439, USA*

[6]*Center for Functional Nanomaterials, Brookhaven National Laboratory, Upton, New York 11793, USA*

Abstract

The temperature-dependent behavior of magnetic domains plays an essential role in the magnetic properties of materials, leading to widespread applications. However, experimental methods to access the three-dimensional (3D) magnetic domain structures are very limited, especially for antiferromagnets. Over the past decades, the spin-orbit Mott insulator iridate Sr_2IrO_4 has attracted particular attention because of its interesting magnetic structure and analogy to superconducting cuprates. Here, we apply resonant x-ray magnetic Bragg coherent diffraction imaging to track the real-space 3D evolution of antiferromagnetic ordering inside a Sr_2IrO_4 single crystal as a function of temperature, finding that the antiferromagnetic domain shows anisotropic changes. The anisotropy of the domain shape reveals the underlying anisotropy of the antiferromagnetic coupling strength within Sr_2IrO_4. These results demonstrate the high potential significance of 3D domain imaging in magnetism research.

Introduction

In magnetic materials, the formation and dynamics of the magnetic domains play a critical role to determine the macroscopic magnetic properties, such as magnetization and magnetic susceptibility [1-3]. Experimental access to mesoscale structures of magnetic materials can provide information about fundamental magnetic interactions [4-8], which may be related to intrinsic topological properties in the quantum matter [4]. An intriguing Ruddlesden-Popper family of layered two-dimensional (2D) antiferromagnetic spin-orbit Mott insulators, the iridate series $Sr_{n+1}Ir_nO_{3n+1}$, presents an interesting new class of frustrated systems, where the spin, orbital, and crystal field interactions conspire to determine the overall electronic configuration [9,10]. Indeed, the single-layer iridate, Sr_2IrO_4, which we study here, already hosts a variety of unconventional magnetism [11]. In Sr_2IrO_4, the narrow electronic band of spin-orbit-split Ir 5*d* states can be further split by the modest on-site Coulomb repulsion to generate an antiferromagnetic Mott insulating state [10,12-14].

The antiferromagnetic Mott ground state of Sr_2IrO_4 can be tuned by different parameters, for example, chemical composition, temperature, strain, and disorder [15,16]. Understanding how magnetic domains respond to the presence of disorder can be detected in their robustness to temperature variations. The structure of Sr_2IrO_4 has been reported to be tetragonal, yet the antiferromagnetic structure breaks this symmetry in the ab-plane which should lead to orthorhombic domains discussed below. However, x-ray magnetic scattering experiments [17] report the formation of a single magnetic domain orientation in crystals of millimeter size. This is probably due to the presence of some residual strain every time the crystal is cooled in the cryostat. Only in the large samples needed for neutron scattering do the crystals adopt an equal mixture of domain orientations [18]. The antiferromagnetic domain sizes reported in these experiments are

all resolution-limited, showing that the antiferromagnetic ordering is strong. As a notoriously difficult task, imaging antiferromagnetic structure is accessible to some existing microscopy techniques, for example, x-ray photoemission electron microscopy [19], spin-polarized scanning tunneling microscopy [20], propagation-based phase contrast technique [21], Bragg ptychography [22], and optical second-harmonic generation technique [23,24]. They mainly provide two-dimensional structure information of magnetic materials. Bragg Coherent Diffractive Imaging (BCDI) is a powerful x-ray technique for imaging nanoscale structures in three dimensions [25,26]. It requires a coherent x-ray beam, available from the undulators of third and fourth generation synchrotron sources, such as the Advanced Photon Source (APS). But even there, a large fraction of the available x-ray flux is lost to preserve the beam coherence and so, until now, it has not been possible to overcome the small resonant magnetic cross-section to image antiferromagnetic materials.

In this work, we use the resonant x-ray magnetic BCDI approach to study the temperature-dependence evolution of the three-dimensional (3D) image of the antiferromagnetic domains within a Sr_2IrO_4 single crystal. The small Sr_2IrO_4 crystal was fabricated by Focused Ion Beam (FIB) milling. Inverted Bragg coherent diffraction images from the crystal show the formation of antiferromagnetic domains when the temperature of the Sr_2IrO_4 crystal is below the Néel transition temperature T_N~230K. Additionally, from reconstructed images, the estimated antiferromagnetic domain size is ~1.1 μm at 120 K and therefore fills the host crystal in the in-plane directions. Upon increasing the temperature, the antiferromagnetic domain is seen to shrink along the c-axis direction, suggesting the anisotropic coupling between the Ir spins.

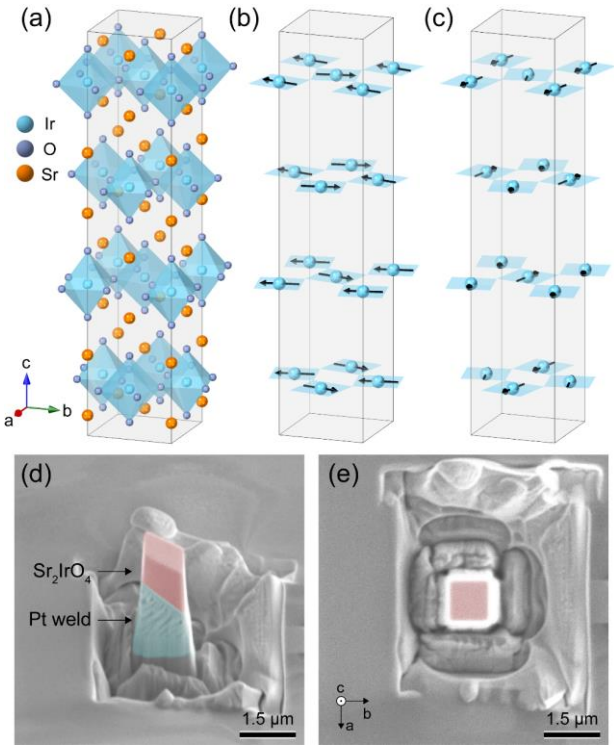

FIG. 1. (a) The crystal structure of Sr_2IrO_4 with space group $I4_1/acd$. (b) *ab* plane canted antiferromagnetic structure. The canting angle of the magnetic moment follows the octahedral rotation rigidly. (c) Corresponding twin domain states of the antiferromagnetic structure. (d) Scanning electron microscopy image of the Sr_2IrO_4 sample from the side view. (e) Top view. The corresponding crystal orientation is indicated in (e).

Sr_2IrO_4 has the classic "214" layered perovskite structural motif with the family of cuprate superconductors. Its lattice constants are $a = b = 5.49$ Å and $c = 25.80$ Å at room temperature with tetragonal symmetry (space group $I4_1/acd$), as shown in Fig. 1(a). In Sr_2IrO_4, the square lattice of Ir^{4+} ions are formed by corner-shared IrO_6 octahedra, which elongate and rotate about the c-axis by $\phi = \sim 11.8°$ [18,27]. Below the Néel temperature T_N ~230 K, the spin-orbital entangled J_{eff} = 1/2 magnetic dipole moments undergo 3D long-range ordering into an orthorhombic antiferromagnetic structure that preserves global inversion symmetry but has lower rotational symmetry. Figure 1(b) and (c) show the two canted antiferromagnetic structures on the IrO_2 planes of Sr_2IrO_4, with the black arrows indicating pseudospins and cyan squares indicating the IrO_2 planes [11,28]. As presented, when the temperature is below T_N, Sr_2IrO_4 has two possible canted

antiferromagnetic structures with the net spin moment along the a- and b-axes, separately [11,29]. These antiferromagnetic structures are related to the 4_1 screw of the Sr_2IrO_4 lattice structure. As a result, the model of twin antiferromagnetic domain states I and II [i.e., with antiferromagnetic structures described by Fig. 1(b) and (c), separately] in Sr_2IrO_4 generate magnetic reflections at $\mathbf{Q}_{\mathrm{I}}$ = (1, 0, 4*n* + 2) and (0, 1, 4*n*) [28], while for domain state II, the magnetic reflections are presented only at $\mathbf{Q}_{\mathrm{II}}$ = (1, 0, 4*n*) and (0, 1, 4*n* + 2).

The high-quality Sr_2IrO_4 single crystal was grown from off-stoichiometric quantities of $SrCl_2$, $SrCO_3$, and IrO_2 using self-flux techniques [29]. To obtain the micro-size crystal needed for the BCDI experiment [30], a large Sr_2IrO_4 crystal was firstly pre-oriented crystallographically using a Laue diffractometer, then a block with its size around 1.2 μm was cut out using the FIB lift-out method (Supplemental Material [31]). Afterward, the obtained Sr_2IrO_4 crystal was welded with Pt onto a silicon wafer as shown in Fig. 1(d)-(e). The selected size of the crystal is less than the penetration depth, ~6.6 μm (Supplemental Material) of 11.218 keV x-ray so that the dynamical diffraction effect is minimized.

The resonant x-ray magnetic BCDI experiment was carried out at the 34-ID-C beamline of the APS, Argonne National Laboratory (Supplemental Material [31]). The incident x-ray energy was tuned to the peak of the magnetic signal at 11.218 keV with π polarization, just below Ir L_3 edge (i.e., the transition from $2p_{3/2}$ to 5*d* state) of the Sr_2IrO_4 crystal. During the measurements, the crystal was mounted on a micro miniature refrigerator (MMR) stage where the temperature was controlled by an MMR K-20 controller. The MMR technology uses a heat exchanger and Joule-Thompson expansion under a fixed flow of high-pressure nitrogen gas [38,39]. Since the Sr_2IrO_4 crystal was pre-aligned before the FIB preparation, the crystal alignment was quickly determined using the crystal (204) and (116) peaks with a six-axis diffractometer to maneuver its orientation.

The coherent diffraction data were collected by rocking the sample. The crystal (116) and antiferromagnetic (106) peaks were used to study the crystal and magnetic structures, separately.

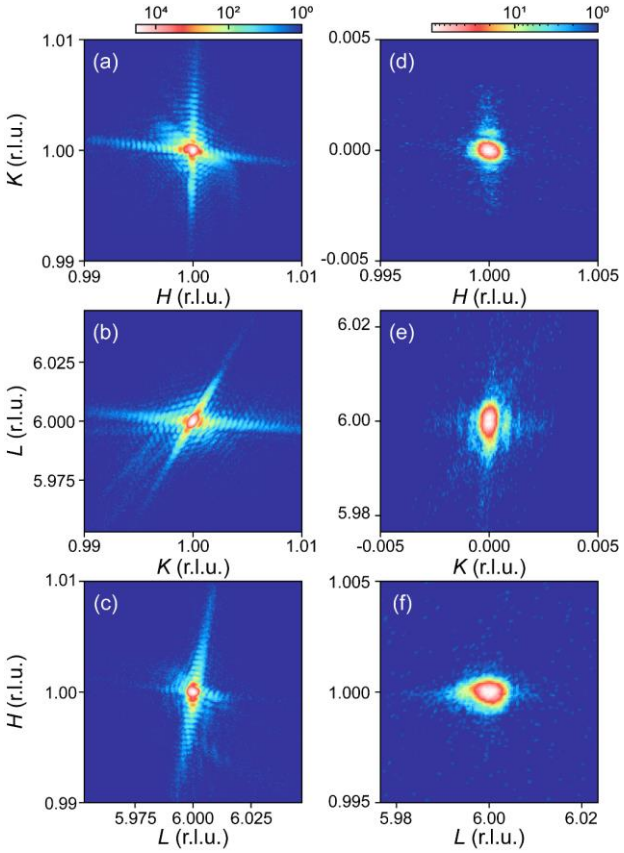

FIG. 2. (a)-(c) Central slice of the 3D reciprocal space mapping around the (116) Bragg peak. (d)-(f) Central slice of the 3D reciprocal space mapping around the antiferromagnetic (106) peak, which was obtained at T=120 K.

Figure 2 shows representative Bragg coherent diffraction patterns of the crystal (116) and antiferromagnetic (106) peaks from the Sr_2IrO_4 crystal, converted into reciprocal lattice unit (r.l.u.) coordinates from the detector coordinates. Here, the reciprocal space is indexed with the tetragonal unit cell, defined as $\mathbf{Q} = \left(\frac{2\pi}{a}H, \frac{2\pi}{b}K, \frac{2\pi}{c}L\right)$. As presented in Fig. 2(a)-(f), these two Bragg coherent x-ray diffraction patterns have different diffraction fringe distributions but similar directions, indicating their distinct sizes and similar facet orientations in real space between the crystal and antiferromagnetic structures. When the crystal is perfect, for the (116) peak, the coherent x-ray

diffraction pattern is mainly determined by the external shape of the crystal. Since the crystal domain size sets an upper limit for the magnetic domain size, the fringe spacings from the antiferromagnetic (106) peak should be similar to or larger than those of the crystal (116) peak.

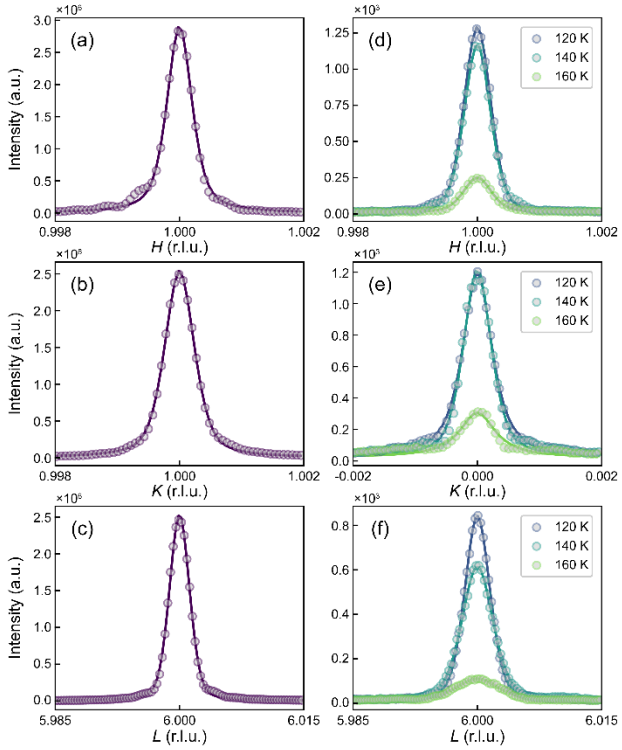

FIG. 3. (a)-(c) Integrated scan intensity for the wave-vector scan along (a) the [*H*, 0, 0], (b) the [0, *K*, 0], and (c) the [0, 0, *L*] directions from the crystal (116) peak. (d)-(f) Corresponding integrated scan intensity from the antiferromagnetic (106) peak at the selected temperatures along different directions.

To explore the effect of temperature on the antiferromagnetic domain in the Sr_2IrO_4 crystal, Fig. 3 shows the integrated x-ray intensity along the [*H*, 0, 0], [0, *K*, 0] and [0, 0, *L*] direction separately from the (106) peak at different selected temperatures and the accompanying (116) peak. Each scan is integrated along the other two transverse r.l.u. directions. As shown in Fig. 3(d)-(f), the antiferromagnetic peak is getting broader along the [0, 0, *L*] direction as the temperature is increasing, indicating the antiferromagnetic domain is shrinking along the c-axis direction. However, changes of the peak width in the other two directions are not apparent. To quantitatively

determine the effect of the temperature on the antiferromagnetic domain, these one-dimensional lineshapes were fitted with Pseudo-Voigt functions. Table I shows the corresponding temperature dependence of the correlation length along the different directions, defined as $\xi = d/\mathrm{FWHM}$, where FWHM represents for full width at half maximum in reciprocal lattice units and d is the lattice spacing of the appropriate reflection.

TABLE I. Correlation lengths of the antiferromagnetic domain along different directions at the selected temperature. Here, the second column shows the correlation length of the host crystal itself by using the crystal (116) peak.

Correlation Length [nm]	(116) peak	120 K	140 K	160 K
ξ_H	1153± 6	1137± 4	1158± 4	1030 ± 13
ξ_K	970 ± 3	1019± 15	1083± 20	871± 54
ξ_L	902± 3	739 ± 2	610 ± 3	423± 9

We consider that the slightly larger value of the correlation length from the antiferromagnetic (106) peak along the [0, *K*, 0] direction at 120 and 140 K than that of the crystal (116) peak, seen in Table I, is due to a slight rotation of the Sr_2IrO_4 crystal under illumination with the highly coherent beam, opposite to the scanning direction, as could also be seen from one scan to the next [40]. However, the effect of crystal movement along the other directions, which are mainly parallel to the detector face, is small. Nevertheless, when the temperature is increased to 160 K, the correlation lengths of the antiferromagnetic domain are decreased along all directions by a different amount. This trend indicates a c-axis to a/b-axis anisotropy of the antiferromagnetic coupling strength along different crystal directions. Specifically, the coupling of spins within the IrO_2 a/b plane is indicated to be stronger than between spins between neighboring planes along the c-axis.

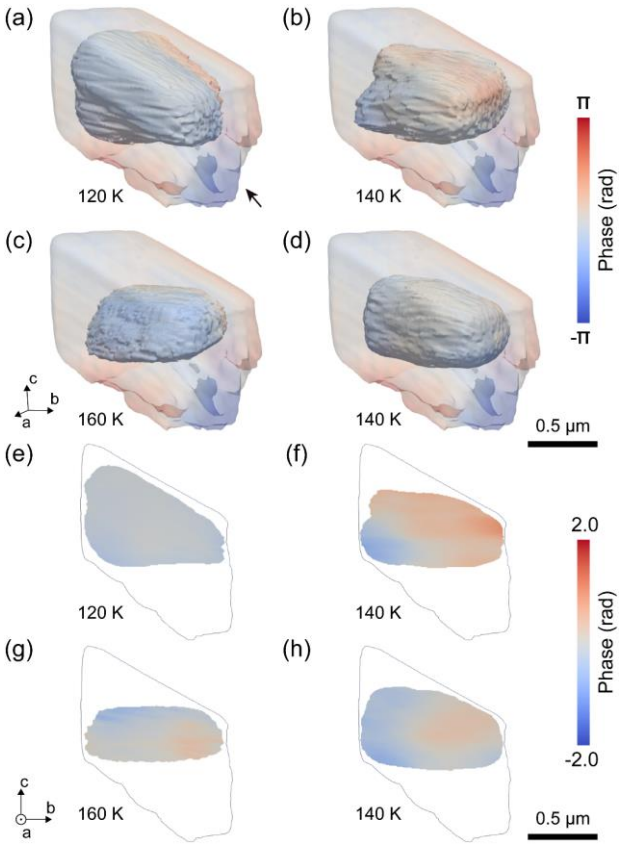

FIG. 4. (a)-(c) Antiferromagnetic domain obtained at T=120, 140, and 160 K, respectively. (d) Antiferromagnetic domain at T=140 K after the thermal cycling. Translucent images of the crystal from the (116) peak and isosurface images from the antiferromagnetic (106) peak are superimposed. (e)-(h) Corresponding center slice of (a)-(c). Here, the black lines show the profile of the Sr_2IrO_4 crystal. The antiferromagnetic images were contoured at 25% of the maximum amplitude and colored according to the image phase at the surface.

Compared with the reciprocal-space data fitting method, real-space images can give new details about the temperature-dependent evolution of the antiferromagnetic domain. Since the data in Fig. 2 and 3 were measured with a coherent x-ray beam, the measured coherent x-ray diffraction patterns can be inverted using the phase retrieval method [35,36]. Figure 4(a)-(c) show the corresponding reconstructed results using the coherent diffraction data from Fig. 2 and 3. Meanwhile, Figure 4(e)-(h) present the corresponding central slice of Fig. 4(a)-(c). As presented in Fig. 4, the translucent isosurface is obtained from the (116) peak at room temperature, while the inside shows the corresponding antiferromagnetic domain at the different temperatures. Compared

with the SEM image in Fig. 1, the missing part below the bottom corner of the reconstruction of the Sr_2IrO_4 crystal, as indicated by the black arrow in Fig. 4(a), is probably due to the sample damage induced by the FIB milling process [41,42]. Also, this region of the crystal is found to contain significant strain, indicated by strong phase values in the complex image, interpreted as a projection of the lattice displacement onto the (116) measurement **Q** vector [25]. This and similar behavior confirmed from another Sr_2IrO_4 crystal (~1.2 μm in size) prepared by the same FIB lift-out method are shown in the Supplemental Material [31]. As the temperature is increasing from 120 K to 160 K, the antiferromagnetic domain shows an anisotropic change. Especially starting from the top corner of the crystal along the c-axis direction, the size of the antiferromagnetic domain decreases much more than other directions. Additionally, the observed antiferromagnetic domains do not occupy the entire volume of the Sr_2IrO_4 crystal, as shown in Fig. 4(a), most notably in the c-axis direction, also seen in Table I. It is possible that these empty regions are filled with the other antiferromagnetic domain orientation, which was not possible to be detected using the (016) peak, due to the limited in-plane rotation angle range of the MMR stage. Therefore, we tried to measure the antiferromagnetic (108) peak of this crystal but could not find any magnetic signal, indicating in these regions the domains with antiferromagnetic spin components along the other direction are too small to be detected or they are not existing. On a larger Sr_2IrO_4 sample (~8 μm in size), it was checked that when the (106) peak appears, the (108) peak of the other domain also appears (Supplemental Material [31]). Thus, as shown in Fig. 4(a), the disappearance of the antiferromagnetic domain in the empty region is possibly related to the strong residual strain induced by the FIB milling process, where the antiferromagnetic domains become orientationally pinned along the b-axis, which cannot be reached. Another possibility is that the strong strain induced by the FIB milling and Pt-welding process suppresses the formation of the

antiferromagnetic domain as a large strain is formed at the bottom corner of the Sr_2IrO_4 crystal. Meanwhile, a weak strain is also observed inside the antiferromagnetic domains, as shown in Fig. 4. While the single antiferromagnetic domain almost fills the crystal in the a- and b-axis directions, there is a negligible morphological change for the domain near the bottom corner of the crystal when changing the temperature from 120K to 160K. Away from the bottom corner of the Sr_2IrO_4 crystal, the shortening of the domain size starting from the top corner of the crystal along the c-axis direction is most probably due to the relatively weaker out-plane spin-spin interaction compared to the in-plane interaction and intrinsic to the iridate compound but may also be caused by the interaction from the small domains at the top corner if existing.

It is hard to know the exact locations of the antiferromagnetic domain in the host Sr_2IrO_4 crystal in Fig. 4, since the two images come from independent measurements. In the a- and b-axis directions, the location is strongly constrained by geometry. But in the c-axis direction, there is uncertainty in both the location and how it changes with temperature. The position is likely to be pinned by the strain fields introduced by the FIB milling process. We explored the pinning effect on the antiferromagnetic domain inside Sr_2IrO_4 sample through thermal cycling experiments. As seen in Fig. 4(d), only one antiferromagnetic domain is formed after thermal cycling, but its shape appears to be slightly rearranged, which suggests that the antiferromagnetic domain is pinned to structural defects in the crystal. However, this could be due to competition between multiple twin domains, resulting in different profiles of the visible antiferromagnetic domain.

Due to the instability of the MMR stage and the limited flux of the third-generation coherent X-ray beam, we consider the current temperature study to be at its limits, based on many repeated attempts to perform the experiment. In the future, with the development of a high-stability cooling stage and upgrading of the APS storage ring and beamline, we hope to use the resonant BCDI

method to investigate the transition of the antiferromagnetic domain in much greater detail to provide insight about the evolution of antiferromagnetic domains near the phase transition. Meanwhile, on a larger length scale, scanning x-ray imaging studies have shown the coexistence of domains with antiferromagnetic spin components along the a- and b-axes in the same crystal, separated by hundreds of microns [6]. Since the isolated Sr_2IrO_4 crystal size can be well-controlled by the FIB milling process, this method will give us a future opportunity to further utilize multiple crystal and antiferromagnetic peaks to study the effect of the intrinsic strain on the formation of the antiferromagnetic domains. Typically, the damage of sample from FIB is ~20 nm with 30-keV ion beam and can be further reduced with lower energy beam. Although a 1-keV ion beam was used for final treatment of our samples to minimize the damage, some of the strains and non-sharp edges could be partly caused by the FIB-milling process.

In conclusion, the resonant x-ray magnetic BCDI method has been applied to study the 3D antiferromagnetic domains inside a small crystal of the spin-orbit Mott insulator Sr_2IrO_4. The results show a distinct anisotropy of the antiferromagnetic domain between the in-plane and c-axis directions. Using the obtained real-space images of the antiferromagnetic domain, the detailed morphological evolution of the antiferromagnetic domain inside the crystal has been studied. Upon increasing the temperature, the single antiferromagnetic domain observed shows an anisotropic change in its domain size. A possible reason for this observation is due to the magnetic anisotropy of strontium iridate, arising from its strong spin-orbit coupling and crystal field effect. Our study demonstrates that by using resonance, BCDI can be extended to the purely magnetic diffraction signals arising from antiferromagnetic ordering. With beamline and coherent source improvements, even finer details of magnetic structure could be investigated inside such a crystal. A quantitative analysis of the structure of the antiferromagnetic domains within a single crystal

can provide important clues about the lattice spin and charge coupling associated with magnetism. The presented approach will find important applications in systems where complex phases give rise to novel physics. We have demonstrated a way to visualize in 3D the antiferromagnetic domains inside an antiferromagnetic material.

Acknowledgments

The work at Brookhaven National Laboratory (BNL) was supported by the U.S. Department of Energy (DOE), Office of Basic Energy Sciences (BES), under Contract No. DESC0012704. The sample was prepared using Focused Ion Beam at the Center for Function Nanomaterials at BNL, which is supported by DOE, BES Users Facility Division. The work at UCL was supported by EPSRC. The measurements were carried out at the Advanced Photon Source (APS) beamline 34-ID-C, which was supported by the DOE, Office of Science, BES, under Contract No. DE-AC02-06CH11357. The beamline 34-ID-C was built with U.S. National Science Foundation grant DMR-9724294. T. A. A. would like to acknowledge support by the DOE, Office of Science, BES, Materials Sciences, and Engineering Division, under Contract DE-AC02-76SF00515. G. C. and H. Z. acknowledge support by NSF via Grants No. DMR 1903888 and DMR 2204811.

*lwu@bnl.gov
†irobinson@bnl.gov

References

[1] P. Nemec, M. Fiebig, T. Kampfrath, and A. V. Kimel, Antiferromagnetic opto-spintronics, Nature Physics **14**, 229 (2018).

[2] I. Gross, W. Akhtar, V. Garcia, L. J. Martinez, S. Chouaieb, K. Garcia, C. Carretero, A. Barthelemy, P. Appel, P. Maletinsky, J. V. Kim, J. Y. Chauleau, N. Jaouen, M. Viret, M. Bibes, S. Fusil, and V. Jacques, Real-space imaging of non-collinear antiferromagnetic order with a single-spin magnetometer, Nature **549**, 252 (2017).

[3] A. Scholl, J. Stohr, J. Luning, J. W. Seo, J. Fompeyrine, H. Siegwart, J. Locquet, F. Nolting, S. Anders, E. E. Fullerton, M. R. Scheinfein, and H. A. Padmore, Observation of antiferromagnetic domains in epitaxial thin films, Science **287**, 1014 (2000).

[4] M. G. Kim, A. Barbour, W. Hu, S. B. Wilkins, I. K. Robinson, M. P. M. Dean, J. Yang, C. Won, S. W. Cheong, C. Mazzoli, and V. Kiryukhin, Real-space observation of fluctuating antiferromagnetic domains, Sci. Adv. **8**, eabj9493 (2022).

[5] Y. Hu, T. Zhang, D. Zhao, C. Chen, S. Ding, W. Yang, X. Wang, C. Li, H. Wang, D. Feng, and T. Zhang, Real-space observation of incommensurate spin density wave and coexisting charge density wave on Cr (001) surface, Nat. Commun. **13**, 445 (2022).

[6] T. Choi, Z. Zhang, H. Kim, S. Park, J. W. Kim, K. J. Lee, Z. Islam, U. Welp, S. H. Chang, and B. J. Kim, Nanoscale Antiferromagnetic Domain Imaging using Full-Field Resonant X-ray Magnetic Diffraction Microscopy, Adv. Mater. **34**, e2200639 (2022).

[7] H. Zhao, Z. Porter, X. Chen, S. D. Wilson, Z. Wang, and I. Zeljkovic, Imaging antiferromagnetic domain fluctuations and the effect of atomic scale disorder in a doped spin-orbit Mott insulator, Sci. Adv. **7**, eabi6468 (2021).

[8] J. Li, J. Pelliciari, C. Mazzoli, S. Catalano, F. Simmons, J. T. Sadowski, A. Levitan, M. Gibert, E. Carlson, J. M. Triscone, S. Wilkins, and R. Comin, Scale-invariant magnetic textures in the strongly correlated oxide $NdNiO_3$, Nat. Commun. **10**, 4568 (2019).

[9] S. J. Moon, H. Jin, K. W. Kim, W. S. Choi, Y. S. Lee, J. Yu, G. Cao, A. Sumi, H. Funakubo, C. Bernhard, and T. W. Noh, Dimensionality-controlled insulator-metal transition and correlated metallic state in 5d transition metal oxides $Sr_{n+1}Ir_nO_{3n+1}$ (n=1, 2, and infinity), Phys. Rev. Lett. **101**, 226402 (2008).

[10] B. J. Kim, H. Jin, S. J. Moon, J. Y. Kim, B. G. Park, C. S. Leem, J. Yu, T. W. Noh, C. Kim, S. J. Oh, J. H. Park, V. Durairaj, G. Cao, and E. Rotenberg, Novel Jeff=1/2 Mott state induced by relativistic spin-orbit coupling in Sr_2IrO_4, Phys. Rev. Lett. **101**, 076402 (2008).

[11] B. J. Kim, H. Ohsumi, T. Komesu, S. Sakai, T. Morita, H. Takagi, and T. Arima, Phase-sensitive observation of a spin-orbital Mott state in Sr_2IrO_4, Science **323**, 1329 (2009).

[12] M. P. Dean, Y. Cao, X. Liu, S. Wall, D. Zhu, R. Mankowsky, V. Thampy, X. M. Chen, J. G. Vale, D. Casa, J. Kim, A. H. Said, P. Juhas, R. Alonso-Mori, J. M. Glownia, A. Robert, J. Robinson, M. Sikorski, S. Song, M. Kozina, H. Lemke, L. Patthey, S. Owada, T. Katayama, M. Yabashi, Y. Tanaka, T. Togashi, J. Liu, C. Rayan Serrao, B. J. Kim, L. Huber, C. L. Chang, D. F. McMorrow, M. Forst, and J. P. Hill, Ultrafast energy- and momentum-resolved dynamics of magnetic correlations in the photo-doped Mott insulator Sr_2IrO_4, Nat. Mater. **15**, 601 (2016).

[13] J. Bertinshaw, Y. K. Kim, G. Khaliullin, and B. J. Kim, Square Lattice Iridates, Annu. Rev. Condens. Matter Phys. **10**, 315 (2019).

[14] C. Martins, M. Aichhorn, L. Vaugier, and S. Biermann, Reduced effective spin-orbital degeneracy and spin-orbital ordering in paramagnetic transition-metal oxides: Sr_2IrO_4 versus Sr_2RhO_4, Phys. Rev. Lett. **107**, 266404 (2011).

[15] E. Paris, Y. Tseng, E. M. Parschke, W. Zhang, M. H. Upton, A. Efimenko, K. Rolfs, D. E. McNally, L. Maurel, M. Naamneh, M. Caputo, V. N. Strocov, Z. Wang, D. Casa, C. W. Schneider, E. Pomjakushina, K. Wohlfeld, M. Radovic, and T. Schmitt, Strain engineering of the charge and spin-orbital interactions in Sr_2IrO_4, Proc. Natl. Acad. Sci. U.S.A. **117**, 24764 (2020).

[16] F. Ye, S. Chi, B. C. Chakoumakos, J. A. Fernandez-Baca, T. Qi, and G. Cao, Magnetic and crystal structures of Sr_2IrO_4: A neutron diffraction study, Phys. Rev. B **87** (2013).

[17] S. Boseggia, H. C. Walker, J. Vale, R. Springell, Z. Feng, R. S. Perry, M. Moretti Sala, H. M. Ronnow, S. P. Collins, and D. F. McMorrow, Locking of iridium magnetic moments to

the correlated rotation of oxygen octahedra in Sr_2IrO_4 revealed by x-ray resonant scattering, J. Condens. Matter Phys. **25**, 422202 (2013).

[18] M. K. Crawford, M. A. Subramanian, R. L. Harlow, J. A. Fernandez-Baca, Z. R. Wang, and D. C. Johnston, Structural and magnetic studies of Sr_2IrO_4, Phys. Rev. B **49**, 9198 (1994).

[19] S. Anders, H. A. Padmore, R. M. Duarte, T. Renner, T. Stammler, A. Scholl, M. R. Scheinfein, J. Stohr, L. Seve, and B. Sinkovic, Photoemission electron microscope for the study of magnetic materials, Rev. Sci. Instrum. **70**, 3973 (1999).

[20] M. Bode, E. Y. Vedmedenko, K. von Bergmann, A. Kubetzka, P. Ferriani, S. Heinze, and R. Wiesendanger, Atomic spin structure of antiferromagnetic domain walls, Nat. Mater. **5**, 477 (2006).

[21] M. G. Kim, H. Miao, B. Gao, S. W. Cheong, C. Mazzoli, A. Barbour, W. Hu, S. B. Wilkins, I. K. Robinson, M. P. M. Dean, and V. Kiryukhin, Imaging antiferromagnetic antiphase domain boundaries using magnetic Bragg diffraction phase contrast, Nat. Commun. **9**, 5013 (2018).

[22] L. Wu, Y. Shen, A. M. Barbour, W. Wang, D. Prabhakaran, A. T. Boothroyd, C. Mazzoli, J. M. Tranquada, M. P. M. Dean, and I. K. Robinson, Real Space Imaging of Spin Stripe Domain Fluctuations in a Complex Oxide, Phys. Rev. Lett. **127**, 275301 (2021).

[23] L. Zhao, D. H. Torchinsky, H. Chu, V. Ivanov, R. Lifshitz, R. Flint, T. Qi, G. Cao, and D. Hsieh, Evidence of an odd-parity hidden order in a spin–orbit coupled correlated iridate, Nat. Phys. **12**, 32 (2015).

[24] K. L. Seyler, A. de la Torre, Z. Porter, E. Zoghlin, R. Polski, M. Nguyen, S. Nadj-Perge, S. D. Wilson, and D. Hsieh, Spin-orbit-enhanced magnetic surface second-harmonic generation in Sr_2IrO_4, Phys. Rev. B **102** (2020).

[25] I. Robinson and R. Harder, Coherent X-ray diffraction imaging of strain at the nanoscale, Nat. Mater. **8**, 291 (2009).

[26] J. Miao, T. Ishikawa, I. K. Robinson, and M. M. Murnane, Beyond crystallography: diffractive imaging using coherent x-ray light sources, Science **348**, 530 (2015).

[27] Q. Huang, J. L. Soubeyroux, O. Chmaissem, I. Natalisora, A. Santoro, R. J. Cava, J. J. Krajewski, and W. F. Peck, Neutron Powder Diffraction Study of the Crystal-Structures of Sr_2RuO_4 and Sr_2IrO_4 at Room-Temperature and at 10-K, J. Solid State Chem. **112**, 355 (1994).

[28] C. Dhital, T. Hogan, Z. Yamani, C. de la Cruz, X. Chen, S. Khadka, Z. S. Ren, and S. D. Wilson, Neutron scattering study of correlated phase behavior in Sr_2IrO_4, Phys. Rev. B **87** (2013).

[29] G. Cao, J. Bolivar, S. McCall, J. E. Crow, and R. P. Guertin, Weak ferromagnetism, metal-to-nonmetal transition, and negative differential resistivity in single-crystal Sr_2IrO_4, Phys. Rev. B **57**, R11039 (1998).

[30] T. A. Assefa, Y. Cao, J. Diao, R. J. Harder, W. Cha, K. Kisslinger, G. D. Gu, J. M. Tranquada, M. P. M. Dean, and I. K. Robinson, Scaling behavior of low-temperature orthorhombic domains in the prototypical high-temperature superconductor $La_{1.875}Ba_{0.125}CuO_4$, Phys. Rev. B **101** (2020).

[31] See Supplemental Material at [URL] for details about sample preparation, x-ray measurements and setup, BCDI reconstruction, strain calculation, penetration depth estimation, comparison of reconstructed Sr_2IrO_4 structures with different sizes,

antiferromagnetic Bragg reflections from the ~8 um sample. The Supplemental Material also contains Refs. [32-37].

[32] M. P. Dean, G. Dellea, R. S. Springell, F. Yakhou-Harris, K. Kummer, N. B. Brookes, X. Liu, Y. J. Sun, J. Strle, T. Schmitt, L. Braicovich, G. Ghiringhelli, I. Bozovic, and J. P. Hill, Persistence of magnetic excitations in $La_{2-x}Sr_xCuO_4$ from the undoped insulator to the heavily overdoped non-superconducting metal, Nat. Mater. **12**, 1019 (2013).

[33] D. Paganin, *Coherent X-ray optics* (Oxford University Press, 2006).

[34] D. Haskel, G. Fabbris, M. Zhernenkov, P. P. Kong, C. Q. Jin, G. Cao, and M. van Veenendaal, Pressure tuning of the spin-orbit coupled ground state in Sr_2IrO_4, Phys. Rev. Lett. **109**, 027204 (2012).

[35] L. Wu, S. Yoo, A. F. Suzana, T. A. Assefa, J. C. Diao, R. J. Harder, W. Cha, and I. K. Robinson, Three-dimensional coherent X-ray diffraction imaging via deep convolutional neural networks, Npj Comput. Mater. **7** (2021).

[36] L. Wu, P. Juhas, S. Yoo, and I. Robinson, Complex imaging of phase domains by deep neural networks, IUCrJ **8**, 12 (2021).

[37] S. Marchesini, H. He, H. N. Chapman, S. P. Hau-Riege, A. Noy, M. R. Howells, U. Weierstall, and J. C. H. Spence, X-ray image reconstruction from a diffraction pattern alone, Phys. Rev. B **68** (2003).

[38] P. Y. Wu and W. A. Little, Measurement of Friction Factors for the Flow of Gases in Very Fine Channels Used for Microminiature Joule-Thomson Refrigerators, Cryogenics **23**, 273 (1983).

[39] H. Geng, X. Y. Cui, J. H. Weng, H. L. She, and W. Q. Wang, Review of experimental research on Joule-Thomson cryogenic refrigeration system, Appl. Therm. Eng. **157** (2019).

[40] M. Monteforte, A. K. Estandarte, B. Chen, R. Harder, M. H. Huang, and I. K. Robinson, Novel silica stabilization method for the analysis of fine nanocrystals using coherent X-ray diffraction imaging, J. Synchrotron Radiat. **23**, 953 (2016).

[41] F. Hofmann, E. Tarleton, R. J. Harder, N. W. Phillips, P. W. Ma, J. N. Clark, I. K. Robinson, B. Abbey, W. Liu, and C. E. Beck, 3D lattice distortions and defect structures in ion-implanted nano-crystals, Sci. Rep. **7**, 45993 (2017).

[42] N. I. Kato, Reducing focused ion beam damage to transmission electron microscopy samples, J. Electron Microsc. (Tokyo) **53**, 451 (2004).